THE JOURNAL OF PHYSICAL CHEMISTRY C
A JOURNAL OF THE AMERICAN CHEMICAL SOCIETY

Open Access
This article is licensed under CC-BY 4.0

pubs.acs.org/JPCC
Article

# Solid-State $^{95}$Mo and $^{93}$Nb NMR Study of $Ba_7Nb_4MoO_{20}$-Based Materials and $Ba_7Ta_{3.7}Mo_{1.3}O_{20.15}$

Masataka Tansho,* Atsushi Goto, Shinobu Ohki, Yuuki Mogami, Yuta Yasui, Yuichi Sakuda, Kotaro Fujii, Takahiro Iijima, and Masatomo Yashima

Cite This: https://doi.org/10.1021/acs.jpcc.4c02645

Read Online

ACCESS | Metrics & More | Article Recommendations | Supporting Information

**ABSTRACT:** Hexagonal perovskite-related oxides, $Ba_7Nb_4MoO_{20}$, $Ba_7Nb_{4-x}Mo_{1+x}O_{20+(1/2)x}$ ($x$ = 0.1), $Ba_7Nb_{4-y}W_yMoO_{20+(1/2)y}$ ($y$ = 0.15), and $Ba_7Ta_{4-z}Mo_{1+z}O_{20+(1/2)z}$ ($z$ = 0.3), have recently been reported to exhibit high oxide-ion and proton conductivity. These materials are of great interest in industrial applications, such as solid oxide fuel cells (SOFCs) and proton ceramic fuel cells (PCFCs) and are known for their unusual structures. Although the structures of $Ba_7Nb_4MoO_{20}$ and their related materials were primarily analyzed by assuming an even distribution of Mo and Nb at each $M$ (=Mo/Nb) site, solid-state nuclear magnetic resonance (NMR) spectra have revealed that Mo and Nb are unevenly distributed in $Ba_7Nb_4MoO_{20}$. As it is crucial to determine whether the contributions to oxide-ion and proton conduction are the same for Mo and Nb, we focused on the signal differences among these as-prepared materials, namely, $Ba_7Nb_4MoO_{20}$, $Ba_7Nb_{3.9}Mo_{1.1}O_{20.05}$, $Ba_7Nb_{3.85}W_{0.15}MoO_{20.075}$, and $Ba_7Ta_{3.7}Mo_{1.3}O_{20.15}$, using solid-state $^{95}$Mo and $^{93}$Nb NMR analysis. The $^{95}$Mo NMR similar predominant peaks revealed in $Ba_7Nb_{3.9}Mo_{1.1}O_{20.05}$, $Ba_7Nb_{3.85}W_{0.15}MoO_{20.075}$, and $Ba_7Ta_{3.7}Mo_{1.3}O_{20.15}$ are also attributed to the $MoO_4$ tetrahedron near the oxide-ion conducting layer owing to the small quadrupolar coupling constant, $|C_Q|$. Furthermore, a minor peak of $^{95}$Mo has been observed in $Ba_7Ta_{3.7}Mo_{1.3}O_{20.15}$, which is presumed to be a $MoO_5$ polyhedron, $MoO_5$ monomer, or $(Mo/Ta)_2O_9$ dimer, formed by the binding of the excess oxygen, represented by $(1/2)z$ ($z$ = 0.3) in the chemical formula. One shoulder peak in the $^{93}$Nb NMR spectrum of $Ba_7Nb_4MoO_{20}$ could be attributed to the $NbO_4$ tetrahedron near the ion conducting layer from its small quadrupolar coupling product, $|P_Q|$, but its intensity is smaller than that considered from the occupancy factors. The small signal intensity is plausible because many are not regular $NbO_4$ tetrahedrons in $Ba_7Nb_4MoO_{20}$. In $Ba_7Nb_{4-x}Mo_{1+x}O_{20+(1/2)x}$ ($x$ = 0.1), the intensity of $NbO_4$ tetrahedron has been further reduced, indicating that the decrease is caused by the transformation of the residual $NbO_4$ tetrahedron to $NbO_5$ polyhedron, $NbO_5$ monomer, or $(Mo/Nb)_2O_9$ dimer, by the binding of excess oxygen, represented by $(1/2)x$ ($x$ = 0.1) in the chemical formula. Thus, the solid-state NMR analysis of the local structure of Mo and Nb oxide polyhedra is a vital tool in analyzing nonstoichiometric ion conductors because it provides information on individual Mo and Nb local structures near the conducting layers of the disordered materials. Therefore, it will potentially contribute to further developing applications using ion conductors.

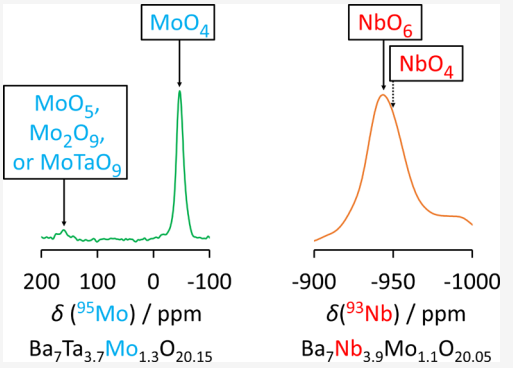


Downloaded via NATL INST FOR MATLS SCIENCE (NIMS) on November 11, 2024 at 08:21:30 (UTC).
See https://pubs.acs.org/sharingguidelines for options on how to legitimately share published articles.

## INTRODUCTION

Oxide-ion and proton conductors are of great interest for industrial applications such as solid oxide fuel cells (SOFCs) and proton ceramic fuel cells (PCFCs).[1−5] Although zirconia-based materials are widely utilized above 700 °C, there remains a strong motivation to find electrolyte materials with higher conductivity that will lower fuel cell operating temperatures to 400−600 °C and reduce costs.[6,7] Improving the conductivity of oxide ions and protons in the bulk requires the detection of the difference in local structures due to each sample.

Among various high ionic conductors, Ba−$M$ (=Mo/Nb(Ta))−O hexagonal perovskites and related materials are promising, and one such case is an oxide-ion conductor, $Ba_3MoNbO_{8.5}$, which exhibits 2.2 × $10^{-3}$ S $cm^{-1}$ at 600 °C.[8] Recently, hexagonal perovskite materials such as $Ba_7Nb_4MoO_{20}$[9−12] and related materials that are mixed conductors of oxide ions and protons have also been reported to exhibit high conductivity, for example, 4.0 × $10^{-3}$ S $cm^{-1}$ at 510 °C of $Ba_7Nb_4MoO_{20}$ (Table 1).[9] The high conductivity can be attributed to the complex structures of these materials. In $Ba_3MoNbO_{8.5}$, the averaged structure is represented as a hybrid of overlapping 9R polytype and palmierite subunits, with one of the $M$ sites in two equivalent positions[13] (Figure

Received: April 23, 2024
Revised: October 11, 2024
Accepted: October 15, 2024

ACS Publications
© XXXX The Authors. Published by American Chemical Society

**Table 1. Total Conductivities of $Ba_7Nb_4MoO_{20}$, $Ba_7Nb_{3.9}Mo_{1.1}O_{20.05}$, $Ba_7Nb_{3.85}W_{0.15}MoO_{20.075}$, and $Ba_7Ta_{3.7}Mo_{1.3}O_{20.15}$**

| materials | $\sigma_{tot}$/S cm$^{-1}$ | temperature (°C) | reference |
|---|---|---|---|
| $Ba_7Nb_4MoO_{20}$ | $4.0 \times 10^{-3}$ | 510 | 9 |
| $Ba_7Nb_{3.9}Mo_{1.1}O_{20.05}$ | $5.8 \times 10^{-4}$ | 310 | 10 |
| $Ba_7Nb_{3.85}W_{0.15}MoO_{20.075}$ | $2.2 \times 10^{-2}$ | 660 | 11 |
| $Ba_7Ta_{3.7}Mo_{1.3}O_{20.15}$ | $1.08 \times 10^{-3}$ | 377 | 12 |

S1). In $Ba_7Nb_4MoO_{20}$ and related materials, the hexagonal (h) and cubic (c) close-packed $BaO_3$ layers and the oxygen-deficient cubic (c′) $BaO_2$ layers are stacked in a (c′hhcchh) sequence[14] (Figure S2). In the first report, it was concluded that Mo/Nb did not exist at the $M(4)$ site at a high temperature of 800 °C in as-prepared $Ba_7Nb_4MoO_{20}$(Figure S2), but several recent reports have shown that a small fraction of Nb exists in the $M(4)$ site at a room temperature,[9,11] which is migrated from the $M(2)$ site (Figures 1 and S3).

The structures of $Ba_3MoNbO_{8.5}$, $Ba_7Nb_4MoO_{20}$, and their related materials were studied mainly using X-ray diffraction, neutron diffraction, and electron diffraction by assuming an even distribution of Mo and Nb at each Mo/Nb site and analyzed as having averaged Mo and Nb atoms.[9−11,15−18] X-rays, neutrons, and electrons have close scattering capabilities, making it difficult to distinguish between Nb and Mo. One of the most significant advantages of solid-state nuclear magnetic resonance (NMR) is the ability to independently observe adjacent elements in the periodic table. In $Ba_3MoNbO_{8.5}$, two $^{93}$Nb and four $^{95}$Mo NMR peaks were detected at the two Mo/Nb sites, indicating an uneven distribution of Mo and Nb within the Mo/Nb sites.[19] In as-prepared $Ba_7Nb_4MoO_{20}$, only one $^{95}$Mo NMR signal was observed. Resonant X-ray diffraction (RXRD) and density-functional theory (DFT) calculations determined that all the Mo was present at the $M(2)O_4$ site near the oxide-ion conducting layer.[20] Finally, the neutron diffraction data were used to refine the occupancy of $M(1)$ to 100% Nb, $M(2)$ to 42% Nb, 50% Mo, and 8% vacancy, $M(3)$ to 100% Nb, and $M(4)$ to 8% Nb and 92% vacancy. Here, the ratio of the number of equivalent positions in a unit cell, $M(1)$:$M(2)$:$M(3)$:$M(4)$, is 1:2:2:2 (Figures 1 and S3).

The difference in the local structure of the oxygen-deficient c′ layer is significant because the oxide-ion conductivity of $Ba_7Nb_{3.9}Mo_{1.1}O_{20.05}$ is several times higher than that of $Ba_7Nb_4MoO_{20}$.[10] Here, for example, in $Ba_7Nb_{4-x}Mo_{1+x}O_{20+(1/2)x}$ ($x$ = 0.1), it is considered that the increase in interstitial O(5) enhances the oxygen-ion conduction (Figure S2). Moreover, neutron scattering length density analyses of $Ba_7Nb_{3.8}Mo_{1.2}O_{20.1}$ indicate that the excess oxygen atoms are incorporated by the formation of both 5-fold-coordinated $(Mo/Nb)O_5$ monomer and its $(Mo/Nb)_2O_9$ dimer with a corner-sharing oxygen atom and that the breaking and reforming of the dimers lead to the high oxide-ion conduction in the oxygen-deficient $BaO_{2.1}$ c′ layer.[21] In a previous study of $Ba_7Nb_4MoO_{20}$, suitable attribution was obtained for the $^{95}$Mo NMR data, but the $^{93}$Nb NMR data were poorly attributed by DFT calculations.[20] However, it is more challenging to perform DFT calculations for non-stoichiometric compounds such as $Ba_7Nb_{3.9}Mo_{1.1}O_{20.05}$, although the supercell method can be used to resolve problems related to site mixing and fractional site occupancy,[22−24] potentially overcoming the highlighted challenges and provide valuable insights into the structure and properties of the material. On the contrary, solid-state NMR has the advantage that each nucleus can be measured independently,[19] making it possible to analyze the local structure of the related nonstoichiometric materials by comparing differences among related materials.

Therefore, in this study, as a relatively quantifiable method, we performed solid-state $^{95}$Mo and $^{93}$Nb one-dimensional magic angle spinning (MAS) NMR measurements of $Ba_7Nb_{4-x}Mo_{1+x}O_{20+(1/2)x}$ ($x$ = 0.1)[10] and $Ba_7Nb_{4-y}W_yMoO_{20+(1/2)y}$ ($y$ = 0.15)[11] to detect the effect of excess oxygen. One-dimensional $^{95}$Mo NMR measurement of $Ba_7Ta_{4-z}Mo_{1+z}O_{20+(1/2)z}$ ($z$ = 0.3)[12] was also performed for comparison because $Ba_7Ta_{4-z}Mo_{1+z}O_{20+(1/2)z}$ ($z$ = 0.3) has more excess oxygen than the other samples of similar crystalline structure. As an accurate two-dimensional (2D) analysis method, we also performed a $^{93}$Nb three-quantum

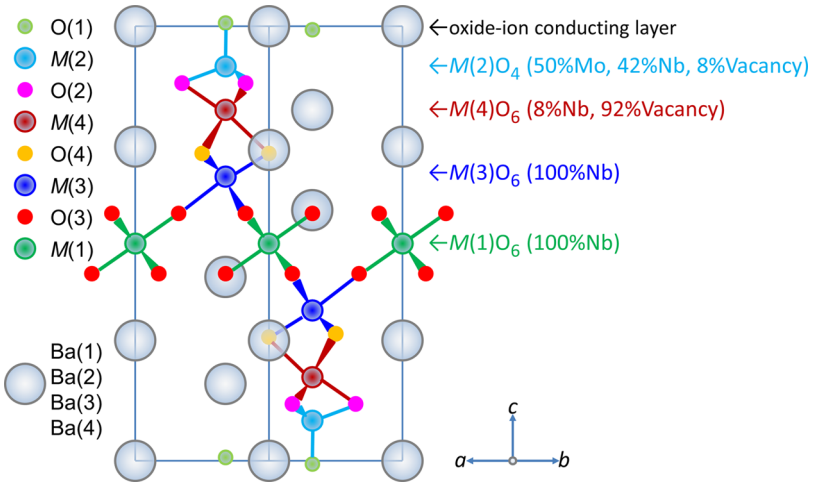


**Figure 1.** Refined crystal structure and site occupancies of Mo and Nb atoms at each $M$ site of $Ba_7Nb_4MoO_{20}\cdot\delta\ H_2O$ at 300 K ($\delta$ = 0.151).[20] The ratio of the number of equivalent positions in a unit cell, $M(1)$:$M(2)$:$M(3)$:$M(4)$, is 1:2:2:2. The position of H and O derived from $\delta\ H_2O$ near the conducting layer is omitted here for simplicity (Figure S3). Initially, the Mo and Nb atoms were assumed to be completely disordered; however, they are considered nearly site-selective.


https://doi.org/10.1021/acs.jpcc.4c02645
J. Phys. Chem. C XXXX, XXX, XXX−XXX

(3Q)MAS NMR measurement,[25] one of the multiple-quantum (MQ) MAS measurements,[26,27] on $Ba_7Nb_{3.9}Mo_{1.1}O_{20.05}$ in addition to the previously measured $Ba_7Nb_4MoO_{20}$.[20] Moreover, the attribution of the $^{93}$Nb signal, which was ambiguously attributed in the previous report, is rediscussed, including the effect of $H_2O$ in $Ba_7Nb_4MoO_{20}$. The differences in NMR measurements by composition may help design high oxide-ion and proton conductors with hexagonal perovskite-related structures.

## EXPERIMENTAL SECTION

**Materials.** Polycrystalline samples of $Ba_7Nb_4MoO_{20}$,[20] $Ba_7Nb_{4-x}Mo_{1+x}O_{20+(1/2)x}$ ($x$ = 0.1),[10] $Ba_7Nb_{4-y}W_yMoO_{20+(1/2)y}$ ($y$ = 0.15),[11] and $Ba_7Ta_{4-z}Mo_{1+z}O_{20+(1/2)z}$ ($z$ = 0.3)[12] were synthesized by the following conventional high-temperature solid-state reactions as already reported.

As previously reported, $Ba_7Nb_4MoO_{20}$ with 0.15 $H_2O$ inside was prepared using the solid-state reaction method.[20] High-purity (>99.9%) $BaCO_3$, $Nb_2O_5$, and $MoO_3$ were mixed as ethanol slurries and ground as dry powders using an agate mortar and pestle. The obtained powder was calcined at 900 °C for 12 h for decarbonation. The obtained material was crushed and ground into a fine powder in an agate mortar and pestle for 1 h as a dried powder and ethanol slurry. The resultant powder was uniaxially pressed at 150 MPa and then sintered in air at 1100 °C for 24 h. The sintered pellet was crushed and ground into a fine powder. The inductively coupled plasma atomic emission spectroscopy (ICP-AES) result indicated that the cation molar ratio of $Ba_7Nb_4MoO_{20}$ was Ba:Nb:Mo = 6.89(12):4.078(18):1.034(10), which is consistent with the nominal composition. The bulk water content of $\delta$ = 0.151(5) was calculated by using the refined occupancy factors in the Rietveld analysis of the neutron diffraction data at 30 K.

$Ba_7Nb_{4-x}Mo_{1+x}O_{20+(1/2)x}$ ($x$ = 0.1) was prepared by the solid-state reactions.[10] High-purity (>99.9%) $BaCO_3$, $Nb_2O_5$, and $MoO_3$ were mixed and ground using an agate mortar and pestle as an ethanol slurry and dry powder repeatedly for 1 h. The obtained mixture was calcined at 900 °C for 12 h in static air. The calcined sample was repeatedly crushed and ground using an agate mortar and pestle as an ethanol slurry and dry powder for 1 h. The powder thus obtained was uniaxially pressed into a pellet at 150 MPa and subsequently sintered in static air at 1100 °C for 24 h. The cation atomic ratio of Ba:Nb:Mo = 7.11(14):3.81(3):1.126(14) for $Ba_7Nb_{3.9}Mo_{1.1}O_{20.05}$ determined through X-ray fluorescence (XRF) analyses agreed with that of the nominal composition where the number in parentheses is the standard deviation in the last digit.

$Ba_7Nb_{4-y}W_yMoO_{20+(1/2)y}$ ($y$ = 0.15) was synthesized via conventional high-temperature solid-state reactions.[11] $BaCO_3$ (99.95%, Kojundo Chemical Laboratory Co.), $Nb_2O_5$ (99.9%, Kojundo Chemical Laboratory Co.), $MoO_3$ (99.98%, Kojundo Chemical Laboratory Co.), and $WO_3$ (99.9%, Kojundo Chemical Laboratory Co.) were weighed according to the ratio and mixed in an agate mortar and pestle as a dry powder and ethanol slurry. The obtained mixture was heated at 900 °C for 12 h in air. The calcined powder was ground, pelletized at approximately 150 MPa, and heated again at 1100 °C for 24 h in static air. Parts of the sintered pellets were crushed and ground into white powders for further measurements. The chemical composition of $Ba_7Nb_{3.85}W_{0.15}MoO_{20.075}$ was investigated through ICP-AES using a Shimadzu ICPS-8100 spectrometer. It showed that the cation ratio of the $y$ = 0.15 sample was Ba:Nb:W:Mo = 7.00(4):3.74(5):0.13(4):1.03(1), which agrees with the nominal ratio for $Ba_7Nb_{3.85}W_{0.15}MoO_{20.075}$.

$Ba_7Ta_{4-z}Mo_{1+z}O_{20+z/2}$ ($z$ = 0.3) was prepared by solid-state reactions using high-purity (>99.9%) $BaCO_3$, $Ta_2O_5$, and $MoO_3$ produced by Kojundo Chemical Laboratory Co. Ltd.[12] The starting material in appropriate molar ratios (Ba:Ta:Mo = 7:3.7:1.3) was mixed and ground in the ball-milling process using a yttria-stabilized zirconia ball. The milled mixture was calcined using $Al_2O_3$ crucibles at 1000 °C for $z$ = 0.3.

$Ba_7Nb_{3.9}Mo_{1.1}O_{20.05}$, $Ba_7Nb_{3.85}W_{0.15}MoO_{20.075}$, and $Ba_7Ta_{3.7}Mo_{1.3}O_{20.15}$ are considered to be solid solutions. They are confirmed as single phases using X-ray and neutron diffraction experiments, and the lattice parameters are changed with the composition. The as-prepared samples contain small amounts of water, just as $Ba_7Nb_4MoO_{20}$ contains 0.15 $H_2O$. All NMR experiments were performed on the as-prepared samples.

**$^{95}$Mo NMR Measurements.** All measurements were performed with a fabricated 3.2 mm single resonance MAS probe for low-resonance-frequency nuclei without temperature control, where the resonance frequency for $^{95}$Mo was 52.16 MHz at 18.79 T. The natural abundance and spin number, $I$, are 15.7% and 5/2, respectively. All samples were filled in sample tubes designed with the same volume and rotated at 20 kHz. A 2.0 M $Na_2MoO_4$ solution was used as a 0 ppm reference for the chemical shifts of $^{95}$Mo. A JEOL ECA 800 NMR spectrometer was used to perform the one-dimensional (1D) measurement of $^{95}$Mo. $^{95}$Mo spectra were acquired with 13,000−22,000 scans using a single pulse of 1.2−1.6 $\mu$s, corresponding to a liquid standard $\pi/6$ pulse with a relaxation delay of 20 s, which is sufficient for the recovery of the prominent peak. In particular, the same experimental conditions, including the accumulation number, are used for $Ba_7Nb_{3.9}Mo_{1.1}O_{20.05}$ as well as $Ba_7Nb_4MoO_{20}$, and measurements of these two samples were obtained continuously. Due to the large background signals detected at shift lower than −1000 ppm, signals were recorded within the range of −1000−1000 ppm.

**$^{93}$Nb NMR Measurements.** All measurements were performed with a fabricated 3.2 mm single resonance MAS probe for high-resonance-frequency nuclei without temperature control, where the resonance frequency for $^{93}$Nb was 195.84 MHz at 18.79 T. The natural abundance and spin number, $I$, are 100% and 9/2, respectively. All samples were filled in sample tubes designed with the same volume and rotated at 20 kHz. One-dimensional measurements at MAS = 15 kHz for $Ba_7Nb_4MoO_{20}$ confirmed which peaks were spinning sidebands. A peak of noncubic solid phase, *Pbcm*, of $NaNbO_3$ (Sanwa Chemical Industry, 99.9%) was set at −1093 ppm as a convenient secondary chemical shift reference of the $^{93}$Nb chemical shift at 18.79 T,[28,29] instead of a saturated solution of $NbCl_5$ in acetonitrile at 0 ppm. Here, the quadrupole coupling constant, $C_Q$, of the *Pbcm* phase of $NaNbO_3$ is reported as 19.5 MHz.[29] JEOL ECZR and ECA 800 NMR spectrometers were used for the 1D and 2D measurements, respectively.

Considering the baseline distortion in the single-pulse $^{93}$Nb MAS NMR measurements (Figure S4), which are usually applied for a rigorous quantitative discussion, one-dimensional $^{93}$Nb spectra were acquired with the spin-echo sequence,[30] which are usually nonquantitative. Here, a radiofrequency


https://doi.org/10.1021/acs.jpcc.4c02645
J. Phys. Chem. C XXXX, XXX, XXX−XXX

pulse with a width of 3.0 $\mu$s, which is the $\pi/2$ pulse of the solid *Pbcm* phase of $NaNbO_3$, was applied for the single-pulse measurements. In the case of quadrupole nuclei, $\pi/2$ pulse lengths are often distributed. Therefore, for quantifiability, pulse lengh dependece of each spectra was checked (Figure S5) before the spin-echo experiments and the reduced pulse lengths of 2.0 $\mu$s as the $\pi/3$ pulse and 4.0 $\mu$s as the $2\pi/3$ pulse were applied instead of the $\pi/2$ pulse and $\pi$ pulse of solid $NaNbO_3$, respectively. The echo delay times were set to 50 $\mu$s under rotor-synchronized spinning conditions at 20 kHz. The effective transverse relaxation time constant, $T_2$*, of $^{93}$Nb was approximately 200 $\mu$s for both $Nb(1)O_6$ and $Nb(3)O_6$ octahedra in $Ba_7Nb_4MoO_{20}$. Placing the center frequency of the measurement at −850 ppm, which is similarly far from the peaks, preserves the quantitativeness among the peaks in the echo experiment. Both single-pulse and spin-echo measurements were performed with a radiofrequency field amplitude of approximately 20 kHz. The spectra were obtained with the same 1024 scans, and the relaxation delay was set to 1 s, which is sufficient for the recovery of the prominent peaks. All of the one-dimensional measurements were performed continuously.

We employed 3QMAS NMR measurement with a three-pulse (2.0, 0.9, and 15 $\mu$s) sequence using a zero-quantum filter, as proposed by Amoureux et al.[26,27] The RF field strength was 100 kHz for the first two pulses and 8 kHz for the third pulse. Here, the spectrum was recorded with 264 transients averaged for each of the 1024 $t_1$ increments of 3.3 $\mu$s and a relaxation delay of 0.2 s, which was sufficient to obtain an adequate signal-to-noise ratio. After that, using the same shearing transformation as already reported, the center of the F1 axis is set to the center of the F2 axis.[19,31,32] Here, in the case that the signals are broadened as in the previously reported disordered materials, $Ba_3MoNbO_{8.5}$ (Figure S1)[19] and $Ba_7Nb_4MoO_{20}{\cdot}0.15\ H_2O$,[20] the analysis of the positions of the experimental resonances ($\delta_{F1}$ and $\delta_{F2}$) in the F1 and F2 dimensions, the isotropic shift, $\delta_{iso}$, and the quadrupolar coupling product, $|P_Q|$, are calculated as

$$\delta_{iso} = \frac{17\delta_{F1} + 10\delta_{F2}}{27} \quad (1)$$

and in the case of $I = 9/2$ as $^{93}$Nb

$$|P_Q| = \left(1224{\cdot}\frac{10}{27}(\delta_{F1} - \delta_{F2})\right)^{1/2} \nu_L{\cdot}10^{-3} \quad (2)$$

Here, $\nu_L$ denotes the Larmor frequency. $|P_Q|$ is related to $|C_Q|$ by

$$|P_Q| = |C_Q|(1 + \eta^2/3)^{1/2} \quad (3)$$

The asymmetry parameter of the electric field gradient, $\eta$, takes values between 0 and 1.

## RESULTS AND DISCUSSION

**$^{95}$Mo NMR.** $^{95}$Mo one-dimensional MAS NMR results are shown in Figure 2, where only one prominent peak due to $Mo(2)O_4$ tetrahedron is observed at approximately −45 ppm in $Ba_7Nb_{3.9}Mo_{1.1}O_{20.05}$ and $Ba_7Nb_{3.85}W_{0.15}MoO_{20.075}$, as well as for $Ba_7Nb_4MoO_{20}$.[20] This is in contrast to some $^{95}$Mo signals observed in $Ba_3MoNbO_{8.5}$, which are presumed to be polyhedra of $MoO_5$ or $MoO_6$ as well as $MoO_4$.[19] The central peak of $Ba_7Nb_{3.9}Mo_{1.1}O_{20.05}$ was approximately 1.3 times higher than that of $Ba_7Nb_4MoO_{20}$ measured under the same experimental conditions. The observed peak positions

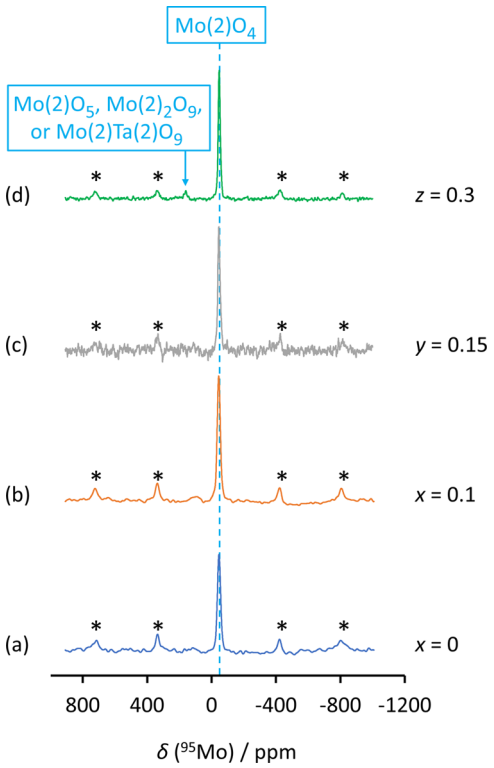


**Figure 2.** $^{95}$Mo MAS NMR spectra of as-prepared (a) $Ba_7Nb_4MoO_{20}$, (b) $Ba_7Nb_{3.9}Mo_{1.1}O_{20.05}$, (c) $Ba_7Nb_{3.85}W_{0.15}MoO_{20.075}$, and (d) $Ba_7Ta_{3.7}Mo_{1.3}O_{20.15}$ measured by the single-pulse method. Panels (a) and (b) were measured under the same conditions, including the number of accumulations. The dashed line is a guide for the eye. Asterisks, *, denote spinning sidebands.

$\delta_{MAS}$, $|C_Q|$, and attributed polyhedron are presented in Table 2, and the DFT results of $Ba_7Nb_4MoO_{20}$ are presented in Table 3. $|C_Q| \leq 2$ MHz of the peaks are also confirmed by a home-written program[33] (Figure S6) in addition to the DMFIT[34] used for $Ba_3MoNbO_{8.5}$. Here, the relationship among $\delta_{MAS}$, isotropic shift, $\delta_{iso}$, and a second-order quadrupolar-induced shift, $\delta_{qis}$, is expressed using the following equation

$$\delta_{MAS} = \delta_{iso} + \delta_{qis} \quad (4)$$

It has already been reported that the signal of $Ba_7Nb_4MoO_{20}$ is assigned to the $MoO_4$ tetrahedron, $Mo(2)O(1)_1O(2)_3$, near the conducting layer.[20] The similar peaks in the as-prepared $Ba_7Nb_{3.9}Mo_{1.1}O_{20.05}$ and $Ba_7Nb_{3.85}W_{0.15}MoO_{20.075}$ are also definitely attributed to the $MoO_4$ tetrahedron, $Mo(2)O(1)_1O(2)_3$, because the shifts and line shapes of the NMR spectra are directly dependent on the local structure and state of the electrons. There is no cubic-centered *M* site in $Ba_7Nb_4MoO_{20}$, but it is a nearly spherical site because it has the smallest $|C_Q|$ value in the calculated model (Table 3). The $^{95}$Mo peak in as-prepared $Ba_7Nb_{3.9}Mo_{1.1}O_{20.05}$ is larger than the $^{95}$Mo peak in $Ba_7Nb_4MoO_{20}$ because the Mo ratio in $Ba_7Nb_{3.9}Mo_{1.1}O_{20.05}$ is 1.1 times larger, and the $Mo(2)O_4$ tetrahedron content ratio is increased (Supporting Information, Note S1).

For $Ba_7Ta_{3.7}Mo_{1.3}O_{20.15}$, in addition to a similar Lorentzian-like peak at −47 ppm, there exists a minor peak at approximately +165 ppm also observed in $Ba_3MoNbO_{8.5}$ at +160 ppm (Figure S1), about one-tenth the height of the maximum peak. The DFT results for $Ba_7Ta_4MoO_{20}$ are presented in Table 4. $Ba_7Ta_{3.7}Mo_{1.3}O_{20.15}$ contains Ta instead


https://doi.org/10.1021/acs.jpcc.4c02645
J. Phys. Chem. C XXXX, XXX, XXX−XXX

Table 2. Experimental $^{95}$Mo Peak Position, Quadrupolar Coupling Constant, and Attributed Polyhedron

| as-prepared samples | $\delta_{MAS}$/ppm[a] | $\lvert C_Q\rvert$/MHz[b] | polyhedron |
|---|---|---|---|
| $Ba_7Nb_4MoO_{20}$ | −47[c] | ≤2[c] | $Mo(2)O_4$[c] |
| $Ba_7Nb_{3.9}Mo_{1.1}O_{20.05}$ | −44 | ≤2 | $Mo(2)O_4$ |
| $Ba_7Nb_{3.85}W_{0.15}MoO_{20.075}$ | −44 | ≤2 | $Mo(2)O_4$ |
| $Ba_7Ta_{3.7}Mo_{1.3}O_{20.15}$ | −47 | ≤2 | $Mo(2)O_4$ |
| $Ba_7Ta_{3.7}Mo_{1.3}O_{20.15}$ | +165 | unclear | $Mo(2)O_5$, $Mo(2)_2O_9$, or $Mo(2)Ta(2)O_9$ |

[a]$\delta_{MAS}$ is the magnetic field-dependent value. Here, the magnetic field is 18.79 T. [b]Simulated by the home-written program[33] (Figure S6) in addition to the DMFIT.[34] [c]Experimental data and attribution for $Ba_7Nb_4MoO_{20}$.[20]

Table 3. Calculated $^{95}$Mo Isotropic Chemical Shift, Quadrupolar Coupling Constant, and Peak Position for Mo−O Polyhedron of $Ba_7Nb_4MoO_{20}$[20]

| models[a] | polyhedron | $\delta_{iso}$ /ppm | $\lvert C_Q\rvert$/MHz | $\delta_{MAS}$ /ppm[b] |
|---|---|---|---|---|
| (4), (5) | $Mo(1)O_6$ | +275 to +277 | 1.47, 2.00 | +269 to +270 |
| (1)−(3), (5) | $Mo(2)O_4$ | −36.5 to −28.4 | 0.36−0.90 | −36.8 to −29.1 |
| (6) | $Mo(3)O_6$ | +164 | 2.87 | +145 |
| (7)−(10) | $Mo(2)O_5$ | +27 to +221 | 5.1−10.7 | −57 to +80 |
| (7), (8) | $Mo(4)O_6$ | +109, +109 | 5.17, 5.23 | +47, +49 |

[a]Each model is shown in Figures S7 and S8.[20] The values of $Mo(2)O_5$ were calculated by constructing models (7)−(10) combining $M(4)O_6$ and $M(2)O_5$ (Figure S8). [b]$\delta_{MAS}$ is a magnetic field-dependent value that was corrected by the author.[35] Here, the magnetic field is 18.79 T.

Table 4. Calculated $^{95}$Mo Isotropic Chemical Shift, Quadrupolar Coupling Constant, and Peak Position for Mo−O Polyhedron of $Ba_7Ta_4MoO_{20}$

| models[a] | polyhedron | $\delta_{iso}$ /ppm | $\lvert C_Q\rvert$/MHz | $\delta_{MAS}$ /ppm |
|---|---|---|---|---|
| (4), (5) | $Mo(1)O_6$ | +289 to +294 | 0.50, 2.3 | +283 to +289 |
| (1)−(3), (5) | $Mo(2)O_4$ | −28.1 to −18.6 | 0.52−0.83 | −29.7 to −19.3 |
| (6)[b] | $Mo(3)O_6$ | +148, +158 | 7.4, 9.5 | −66 to +2.5 |

[a]Each model is shown in Figure S9. The $M(4)O_6$ octahedron used to construct the model for the $M(2)O_5$ polyhedron in $Ba_7Nb_4MoO_{20}$ does not exist in $Ba_7Ta_{3.7}Mo_{1.3}O_{20.15}$, so calculations similar to those in Table 3 for the $Mo(2)O_5$ polyhedron were not performed for $Ba_7Ta_4MoO_{20}$.[12] [b]Two sets of values were obtained for the same model because there were two minima instead of one.

of Nb at the $M$ sites, but the Lorentzian-like narrow peak must still be owing to the similar $Mo(2)O_4$ tetrahedron because the NMR parameters are strongly dependent on the local structure, and the peak position is hardly affected when $\lvert C_Q\rvert$ is small. The minor peak is considered as follows. As reported earlier, all the Mo is at the $M(2)$ site.[12] In addition, the +165 ppm shift is close to neither +283 to +289 ppm calculated for the $Mo(1)O_6$ octahedron nor −66 to +2.5 ppm calculated for the $Mo(3)O_6$ octahedron in $Ba_7Ta_4MoO_{20}$. Therefore, both $Mo(1)O_6$ and $Mo(3)O_6$ octahedra are unsuitable for attribution of the minor peak. Then, this peak is possibly a signal of the $Mo(2)O_5$ monomer near the conducting layer owing to the extra oxygen involved in the chemical formula $(1/2)z$ ($z$ = 0.3). Here, the possibility of the $M_2O_9$ dimer, $(Mo/Ta)(2)_2O_9$ dimer, should also be considered because the $(Mo/Nb)(2)_2O_9$ dimer with a corner-sharing oxygen atom is indicated for $Ba_7Nb_{3.8}Mo_{1.2}O_{20.1}$.[21] The shifts of $Mo(2)_2O_9$ and $Mo(2)Ta(2)O_9$ dimers could be different from that of the $Mo(2)O_5$ monomer because the electronic state of the Mo of $Mo(2)_2O_9$ and $Mo(2)Ta(2)O_9$ dimers must not be the same as that of the $Mo(2)O_5$ monomer. Therefore, the minor peak of $Ba_7Ta_{3.7}Mo_{1.3}O_{20.15}$ could be a $Mo(2)O_5$ monomer, $Mo(2)_2O_9$ homodimer, or $Mo(2)Ta(2)O_9$ heterodimer.

Unlike $Ba_7Ta_{3.7}Mo_{1.3}O_{20.15}$, no minor peak was observed in as-prepared $Ba_7Nb_{3.9}Mo_{1.1}O_{20.05}$ and $Ba_7Nb_{3.85}W_{0.15}MoO_{20.075}$. Here, we consider the following two reasons: $Mo(2)O_5$ polyhedra, $Mo(2)O_5$ monomer, or $(Mo/Nb)(2)_2O_9$ dimer have not been observed, although $Mo(2)O_5$ polyhedra should exist owing to excess oxygen. First, the excess amounts of oxygen atoms $(1/2)x$ ($x$ = 0.1) of $Ba_7Nb_{3.9}Mo_{1.1}O_{20.05}$ and $(1/2)y$ ($y$ = 0.15) of $Ba_7Nb_{3.85}W_{0.15}MoO_{20.075}$ are only 1/3 and 1/2 of $(1/2)z$ ($z$ = 0.3) of $Ba_7Ta_{3.7}Mo_{1.3}O_{20.15}$, respectively. Second, the line width of the quadrupole second-order perturbation is known to depend on $\lvert C_Q\rvert^2$,[36] and the peak height depends on $\lvert C_Q\rvert^{-2}$. Because the calculated $\lvert C_Q\rvert$ of the $Mo(2)O_5$ monomer is larger than that of the $Mo(2)O_4$ tetrahedron (Table 3), the signal height of the $Mo(2)O_5$ monomer must become much smaller than that of the $Mo(2)O_4$ tetrahedron (Figure S10). Similarly, the signal height of the $(Mo/Nb)(2)_2O_9$ dimer is possibly much smaller than that of the $Mo(2)O_4$ tetrahedron because $\lvert C_Q(^{95}Mo)\rvert$ of the $(Mo/Nb)(2)_2O_9$ dimer is likely larger than that of $Mo(2)O_4$, which is the smallest in Table 3.

**$^{93}$Nb NMR.** Figure 3 compares one-dimensional MAS NMR measurements of $^{93}$Nb under the same experimental conditions

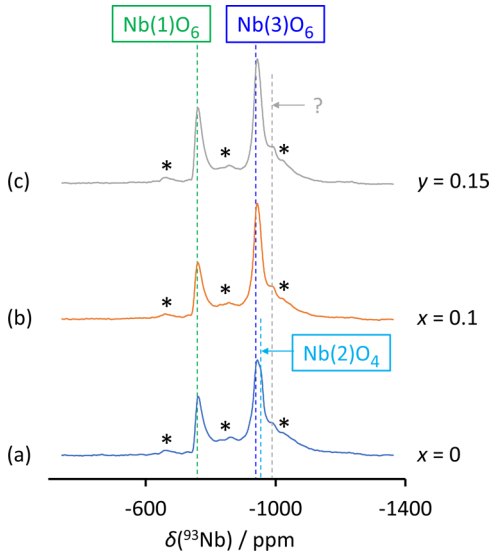


Figure 3. $^{93}$Nb MAS NMR spectra of (a) $Ba_7Nb_4MoO_{20}$, (b) $Ba_7Nb_{3.9}Mo_{1.1}O_{20.05}$, and (c) $Ba_7Nb_{3.85}W_{0.15}MoO_{20.075}$ measured by the spin-echo method under the same conditions, including the number of accumulations. The dashed lines are eye guides. Asterisks, *, denote spinning sidebands. Here, 1D measurements at MAS = 15 kHz for $Ba_7Nb_4MoO_{20}$ confirmed which peaks were spinning sidebands.


https://doi.org/10.1021/acs.jpcc.4c02645
J. Phys. Chem. C XXXX, XXX, XXX−XXX

**Table 5. $^{93}$Nb Peak Position, $\delta_{MAS}$, Measured by $^{93}$Nb 1D MAS NMR Using the Spin-Echo Method, $^{93}$Nb $\delta_{iso}$ and $|P_Q|$ Determined by $^{93}$Nb 3QMAS NMR, and Attributed Polyhedron**

| as-prepared samples | $\delta_{MAS}$/ppm[a] | $\delta_{iso}$ /ppm[b] | $\|P_Q\|$/MHz[b] | polyhedron |
|---|---|---|---|---|
| $Ba_7Nb_4MoO_{20}$ | −762[c] | −748[c] | 15[c] | $Nb(1)O_6$ |
| $Ba_7Nb_4MoO_{20}$ | −944[c] | −928[c] | 19[c] | $Nb(3)O_6$ |
| $Ba_7Nb_4MoO_{20}$ | −950[c] | −952[c] | 6[c] | $Nb(2)O_4$ |
| $Ba_7Nb_{3.9}Mo_{1.1}O_{20.05}$ | −761 | −746 | 20 | $Nb(1)O_6$ |
| $Ba_7Nb_{3.9}Mo_{1.1}O_{20.05}$ | −944 | −934 | 18 | $Nb(3)O_6$ |
| $Ba_7Nb_{3.85}W_{0.15}MoO_{20.075}$ | −761 | | | $Nb(1)O_6$ |
| $Ba_7Nb_{3.85}W_{0.15}MoO_{20.075}$ | −944 | | | $Nb(3)O_6$ |

[a]$\delta_{MAS}$ is the magnetic field-dependent value. Here, the magnetic field is 18.79 T. [b]$\delta_{iso}$ and $|P_Q|$ calculated by eqs 1 and 2 are magnetic field-independent values. [c]Experimental data and attribution for $Ba_7Nb_4MoO_{20}$.[20]

as the spin-echo method. The peak positions in this figure and Table 5, $\delta_{MAS}$, were determined from the spin-echo[30] results (Figure 3) as previously reported[20] for $Ba_7Nb_4MoO_{20}$ to avoid the baseline distortion often seen with single-pulse methods (Figure S4). The $\delta_{MAS}$ and the attributed polyhedron compared with DFT calculations (Table 6) are listed in Table 5, along with the results of two-dimensional experiments shown later. The previous attribution of the two peaks, −762 ppm for $Nb(1)O_6$ octahedron and −950 ppm for $Nb(2)O_4$ tetrahedron, was the opposite of the usual octahedron−tetrahedron attribution,[28,37] so this attribution remained an estimate.[20] Similar prominent peaks at −761 and −944 ppm were observed in both $Ba_7Nb_{3.9}Mo_{1.1}O_{20.05}$ and $Ba_7Nb_{3.85}W_{0.15}MoO_{20.075}$. Both $Ba_7Nb_{3.9}Mo_{1.1}O_{20.05}$ and $Ba_7Nb_{3.85}W_{0.15}MoO_{20.075}$ have increased peak heights at −944 ppm. Conversely, the height of the −950 ppm peak, which appeared close to the −944 ppm peak in $Ba_7Nb_4MoO_{20}$, decreased sharply in $Ba_7Nb_{3.9}Mo_{1.1}O_{20.05}$ and $Ba_7Nb_{3.85}W_{0.15}MoO_{20.075}$. Moreover, the small peak at −990 ppm in $Ba_7Nb_4MoO_{20}$, which was suggested to be $Nb(2)O_5$ polyhedron or $Nb(4)O_6$ octahedron in a previous work[20] but whose shift could not be well explained, is also observed in $Ba_7Nb_{3.9}Mo_{1.1}O_{20.05}$ and $Ba_7Nb_{3.85}W_{0.15}MoO_{20.075}$.

Figure 4 shows the $^{93}$Nb two-dimensional 3QMAS NMR result for $Ba_7Nb_{3.9}Mo_{1.1}O_{20.05}$ and the previously reported result for $Ba_7Nb_4MoO_{20}$. Here, the peak on −761 ppm is spread to the quadrupole-induced shift axis direction, and the peak on −944 ppm is spread to both quadrupole-induced shift and chemical shift axis direction[19,32] in the same manner. Therefore, the $\delta_{iso}$ and $|P_Q|$ were obtained from this figure using eqs 1 and 2 for disordered materials' analysis and are listed in Table 5. Here, in $Ba_7Nb_{3.9}Mo_{1.1}O_{20.05}$, there is no significant change in the two spots farther from the diagonal line corresponding to the larger $|P_Q|$ peaks, whereas the spot nearest the diagonal line that corresponds to the smallest $|P_Q|$ peak has almost disappeared. In other words, the corresponding component for the smallest $|P_Q|$ peak in Figure 3a is sharply decreased in $Ba_7Nb_{3.9}Mo_{1.1}O_{20.05}$.

Here, the −952 ppm spot in $Ba_7Nb_4MoO_{20}$ was suggested to be a $NbO_4$ tetrahedron at the $M(2)$ site in the previous report because the 6 MHz of $|P_Q$ ($^{93}$Nb)| could only be explained by the smallest calculated case (Table 6).[20,35] This estimation is reasonable because the $|C_Q$ ($^{95}$Mo)| value of the similar $MO_4$ tetrahedron at the same $M(2)$ site also corresponds to the smallest calculated values (Table 3).

For the two sites at −762 and −944 ppm of $Ba_7Nb_4MoO_{20}$, when both peaks are all Nb and attributed to $M(1)$ and $M(3)$,

**Table 6. Calculated $^{93}$Nb Isotropic Chemical Shift, Quadrupolar Coupling Product, and Peak Position for Nb−O Polyhedron of $Ba_7Nb_4MoO_{20}$[20]**

| models[a] | polyhedron | $\delta_{iso}$ /ppm | $\|P_Q\|$/MHz | $\delta_{MAS}$/ppm[b] |
|---|---|---|---|---|
| (1), (2), (3) | $Nb(1)O_6$ | −800 to −810 | 18−20 | −812 to −825 |
| (1), (2), (3) | $Nb(2)O_4$ | −848 to −862 | 6.8−18 | −858 to −864 |
| (1), (2), (3) | $Nb(3)O_6$ | −867 to −897 | 41−50 | −929 to −988 |
| (9), (10) | $Nb(2)O_5$ | −803, −812 | 43, 75 | −884, −1044 |
| (9), (10) | $Nb(4)O_6$ | −845, −858 | 71, 73 | −1028, −1052 |

[a]Each model is shown in Figures S7 and S8.[20] Here, the models with Mo atoms at the $M(2)$ site were used. [b]$\delta_{MAS}$ is a magnetic field-dependent value that was corrected by the author.[35] Here, the magnetic field is 18.79 T.

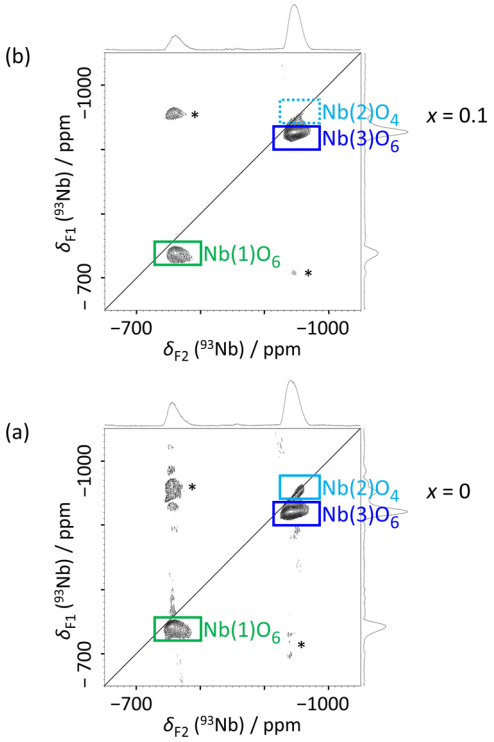


**Figure 4.** $^{93}$Nb 3QMAS NMR spectra of as-prepared (a) $Ba_7Nb_4MoO_{20}$ and (b) $Ba_7Nb_{3.9}Mo_{1.1}O_{20.05}$ measured under the same condition. The diagonal line in the 2D diagram is called the chemical shift axis. The spread of the signal along the diagonal line indicates the distribution of the chemical shift when an appropriate shearing transformation is used. The color squares are eye guides. Asterisks, *, denote spinning sidebands.


https://doi.org/10.1021/acs.jpcc.4c02645
J. Phys. Chem. C XXXX, XXX, XXX−XXX

respectively, the peak at −944 ppm should be approximately 1.2 times higher than the peak at −762 ppm related to the ratio of the number of equivalent positions in a unit cell and the result of the $|P_Q|$ difference. Therefore, Figure 3a reflects the equivalent positions' ratio well (Supporting Information, Note S2). Similarly, for the two sites at −761 and −944 ppm of $Ba_7Nb_{3.9}Mo_{1.1}O_{20.05}$, when both peaks are all Nb and are attributed to $M(1)$ and $M(3)$, respectively, the peak at −944 ppm should be approximately 2.5 times higher than the peak at −761 ppm. Therefore, Figure 3b also reflects the quantity ratio well (Supporting Information, Note S3). Thus, the previous estimation that −762 ppm corresponds to the $Nb(1)O_6$ octahedron and −944 ppm corresponds to the $Nb(3)O_6$ octahedron is correct.[20] Since the DFT results support these unusual shifts, the anomalous Nb shifts, which differ from many materials, are probably the result of the coexistence with Mo. The difference between the experimental and the calculated values of $|P_Q|$ in the $Nb(3)O_6$ octahedron may be caused by the effect of molecular motion, which is usually ignored in DFT calculations, or the effect from $H_2O$, which is not considered in this calculation.

Here, if all of the Nb at the $M(2)$ site were formed as a $Nb(2)O_4$ tetrahedron, the area intensity of the $Nb(2)O_4$ tetrahedron in Figure 3a should be 0.84 times that of the $Nb(1)O_6$ octahedron (Supporting Information, Note S4). Since the signal of the $Nb(2)O_4$ tetrahedron must be more intense than $Nb(1)O_6$ and $Nb(3)O_6$ owing to the narrowest line width related to the smallest $|P_Q|$ in Table 5, the peak height is likely the highest among three peaks as shown in Figure S11(a-1). However, the peak height of the $Nb(2)O_4$ tetrahedron obtained in the 1D measurement is smaller than that of the $Nb(3)O_6$ octahedron (Figure 3a), and the area intensity is not 0.84 but 0.50 times that of the $Nb(1)O_6$ octahedron, as shown in Figure S11(a-2). This is presumably because in $Ba_7Nb_4MoO_{20}$, some of the Nb oxide polyhedra at the $M(2)$ site are not regular $Nb(2)O_4$ tetrahedrons due to the bonding of H or O derived from $H_2O$ inside the as-prepared sample.

When Nb is 8% at the $M(4)$ site and all Mo is at the $M(2)$ site also for $Ba_7Nb_{3.9}Mo_{1.1}O_{20.05}$ and $Ba_7Nb_{3.85}W_{0.15}MoO_{20.075}$ as $Ba_7Nb_4MoO_{20}$ (Figure 1), the Nb content ratio of the $M(2)$ sites of $Ba_7Nb_4MoO_{20}$, $Ba_7Nb_{3.9}Mo_{1.1}O_{20.05}$, and $Ba_7Nb_{3.85}W_{0.15}MoO_{20.075}$ is 0.84:0.74:0.8085 (Supporting Information, Note S5). Therefore, the significant decrease in the $^{93}$Nb signal of the $Nb(2)O_4$ tetrahedra in $Ba_7Nb_{3.9}Mo_{1.1}O_{20.05}$ (Figure 3b) and $Ba_7Nb_{3.85}W_{0.15}MoO_{20.075}$ (Figure 3c) cannot be explained as a difference in the ratio of total Nb contained. A reasonable explanation is that the excess amounts of oxygen atoms $(1/2)x$ ($x$ = 0.1) or $(1/2)y$ ($y$ = 0.15) changes $Nb(2)O_4$ tetrahedron to $Nb(2)O_5$ polyhedron, $NbO_5$ monomer or $(Mo/Nb)(2)_2O_9$ dimer, and is no longer $Nb(2)O_4$ tetrahedron.

The −990 ppm peak, suggested as a possible $Nb(2)O_5$ or $Nb(4)O_6$ peak in the earlier report,[20] can be considered as follows. In $Ba_7Nb_4MoO_{20}$, the small signal intensity of $Nb(2)O_4$ tetrahedron is possibly caused by the effect of H and O derived from 0.15 $H_2O$. Therefore, as the third candidate, for example, $Nb(2)O_n$ ($n$ = 4, 5, and 6) polyhedra accompanied by H should be considered for $Ba_7Nb_4MoO_{20}$, $Ba_7Nb_{3.9}Mo_{1.1}O_{20.05}$, and $Ba_7Nb_{3.85}W_{0.15}MoO_{20.075}$. Therefore, the attribution of the −990 ppm peak will be investigated in future research.

## CONCLUSIONS

$Ba_7Nb_4MoO_{20}$ and related materials are of great interest for industrial applications such as solid oxide fuel cells, proton ceramic fuel cells, gas sensors, and oxygen-separation membranes because they exhibit high oxide-ion and proton conductivity. These materials are considered with respect to the mixed oxide coordination number on $M(2)$ sites near the oxide-ion conducting layer. Initially, the structures of $Ba_7Nb_4MoO_{20}$ and their related materials were mostly analyzed by assuming an even distribution of Mo and Nb at each site. However, in the previous report, a combination of several techniques, including solid-state NMR, showed that in $Ba_7Nb_4MoO_{20}$, most Mo, unlike Nb, is located at the $M(2)$ site near the ion conducting layer, since in $^{95}$Mo NMR only one signal was observed. Because of the peak position and the small $|C_Q|$ value, the signal was attributed to the $MoO_4$ tetrahedron. To obtain more information, solid-state NMR is promising because the signal intensity, line width, and shift are directly affected by differences in the local structure, and the intensity ratio of each peak reflects the amount ratio. This method circumvents the difficulty of distinguishing Nb and Mo near the oxide-ion and proton conducting layers using many analytical methods (Figure S2). This is the first experimental study on hexagonal perovskite $Ba_7Nb_4MoO_{20}$-related materials, with a focus on the differences in NMR signals near the oxide-ion conducting layer in different materials. As well $Ba_7Nb_4MoO_{20}$, the sharp Lorentzian-like $^{95}$Mo NMR peaks revealed in $Ba_7Nb_{3.9}Mo_{1.1}O_{20.05}$, $Ba_7Nb_{3.85}W_{0.15}MoO_{20.075}$, and $Ba_7Ta_{3.7}Mo_{1.3}O_{20.15}$ are also definitely attributed to the $Mo(2)O_4$ tetrahedron near the oxide-ion conducting layer owing to the shifts and the small $|C_Q|$ values. Moreover, in $Ba_7Ta_{4-z}Mo_{1+z}O_{20+(1/2)z}$, an extra $^{95}$Mo peak of $Mo(2)O_5$, $Mo(2)_2O_9$, or $Mo(2)Ta(2)O_9$ polyhedra was observed, which is possibly related to the excess amounts of oxygen atoms $(1/2)z$ ($z$ = 0.3). The results for $^{93}$Nb differ significantly from those for $^{95}$Mo. The $^{93}$Nb NMR peak associated with the $Nb(2)O_4$ tetrahedron of $Ba_7Nb_4MoO_{20}$ has a small $|P_Q|$, so it should be quite sensitive to its amount, as should the $^{95}$Mo peak of the $Mo(2)O_4$ tetrahedron, which also has a small $|C_Q|$. However, 0.50 of the $^{93}$Nb NMR signal intensity associated with the $Nb(2)O_4$ tetrahedron of $Ba_7Nb_4MoO_{20}$ is considerably smaller than 0.84 of the $Nb(1)O_6$ signal intensity despite 0.84 of the composition ratio at the $M(2)$ site. Therefore, some of the Nb in the $M(2)$ site is no longer a regular $NbO_4$ tetrahedron, possibly owing to H or O derived from 0.15 $H_2O$ in as-prepared $Ba_7Nb_4MoO_{20}$. Furthermore, the $^{93}$Nb NMR peak intensities associated with the $Nb(2)O_4$ tetrahedra of $Ba_7Nb_{3.9}Mo_{1.1}O_{20.05}$ and $Ba_7Nb_{3.85}W_{0.15}MoO_{20.075}$ were reduced compared to $Ba_7Nb_4MoO_{20}$. This reduction must be caused by the bonding of excess amounts of oxygen atoms on the $Nb(2)O_4$ tetrahedron related with $(1/2)x$ ($x$ = 0.1) or $(1/2)y$ ($y$ = 0.15). That is, in $Ba_7Nb_4MoO_{20}$, while observing a prominent $MoO_4$ tetrahedral signal, some of the Nb(2)−O polyhedra are not $Nb(2)O_4$ tetrahedron, possibly due to the bonding of H or O derived from $H_2O$ inside the as-prepared sample. Moreover, the effects of excess oxygen related to $(1/2)x$, $(1/2)y$, or $(1/2)z$ are found in both $Mo(2)O_4$ and $Nb(2)O_4$ tetrahedra near the oxide-ion conducting layer for $Ba_7Nb_{4-x}Mo_{1+x}O_{20+(1/2)x}$ ($x$ = 0.1), $Ba_7Nb_{4-y}W_yMoO_{20+(1/2)y}$ ($y$ = 0.15), and $Ba_7Ta_{4-z}Mo_{1+z}O_{20+(1/2)z}$ ($z$ = 0.3). Thus, solid-state NMR enables local structural analysis of individual Mo and Nb atoms in solid solutions and offers immense potential


https://doi.org/10.1021/acs.jpcc.4c02645
J. Phys. Chem. C XXXX, XXX, XXX−XXX

for the electrolyte design of many perovskite derivatives, especially related systems containing Mo/Nb atoms.

## ■ ASSOCIATED CONTENT

### Supporting Information

The Supporting Information is available free of charge at https://pubs.acs.org/doi/10.1021/acs.jpcc.4c02645.

Eleven figures, five notes on the comparison of $Mo(2)O_4$ peak intensity, −762 and −944 ppm $^{93}$Nb peak height ratios of $Ba_7Nb_4MoO_{20}$, −761 and −944 ppm $^{93}$Nb peak height ratios of $Ba_7Nb_{3.9}Mo_{1.1}O_{20.05}$, the ratio of the numbers of equivalent crystallographic sites in a unit cell, and Nb amount ratio of the $M(2)$ site (PDF)

## ■ AUTHOR INFORMATION


### Corresponding Author

**Masataka Tansho** − *National Institute for Materials Science (NIMS), Tsukuba 305-0003, Japan*; orcid.org/0000-0001-7986-3199; Email: TANSHO.Masataka@nims.go.jp

### Authors

**Atsushi Goto** − *National Institute for Materials Science (NIMS), Tsukuba 305-0003, Japan*

**Shinobu Ohki** − *National Institute for Materials Science (NIMS), Tsukuba 305-0003, Japan*

**Yuuki Mogami** − *National Institute for Materials Science (NIMS), Tsukuba 305-0003, Japan*

**Yuta Yasui** − *Department of Chemistry, School of Science, Institute of Science Tokyo, Tokyo 152-8551, Japan*

**Yuichi Sakuda** − *Department of Chemistry, School of Science, Institute of Science Tokyo, Tokyo 152-8551, Japan*

**Kotaro Fujii** − *Department of Chemistry, School of Science, Institute of Science Tokyo, Tokyo 152-8551, Japan*; orcid.org/0000-0003-3309-9118

**Takahiro Iijima** − *Institute of Arts and Sciences, Yamagata University, Yamagata 990-8560, Japan*

**Masatomo Yashima** − *Department of Chemistry, School of Science, Institute of Science Tokyo, Tokyo 152-8551, Japan*; orcid.org/0000-0001-5406-9183

Complete contact information is available at: https://pubs.acs.org/10.1021/acs.jpcc.4c02645


### Author Contributions

The manuscript was written with contributions from all authors. All authors have approved the final version.


### Funding

This work was partly supported by Grants-in-Aid for Scientific Research (KAKENHI, JP21K18182, and JP19H00821) from MEXT.


### Notes

The authors declare no competing financial interest.

## ■ ACKNOWLEDGMENTS


The authors thank Dr. T. Shimizu and K. Deguchi of NIMS for their help with NMR measurements, and this work was supported by the Research Network and Facility Services Division in NIMS. The authors also thank Y. Shimoikeda of Jeol Resonance Inc. for his help with the MQMAS analysis and Y. Suzuki for the helpful discussion and assistance in the experiments/analyses. The authors acknowledge T. Shibata of Kojundo Chemical Laboratory Co. for the ICP measurements and for supplying chemical materials.


## ■ ABBREVIATIONS

NMR, nuclear magnetic resonance; SOFCs, solid oxide fuel cells; PCFCs, proton ceramic fuel cells; RXRD, resonant X-ray diffraction; DFT, density-functional theory; ICP-AES, inductively coupled plasma atomic emission spectroscopy; XRF, X-ray fluorescence; MAS, magic angle spinning; 3Q, three-quantum; MQ, multiquantum

## ■ REFERENCES


(1) Staffell, I.; Scamman, D.; Velazquez Abad, A.; Balcombe, P.; Dodds, P. E.; Ekins, P.; Shah, N.; Ward, K. R. The Role of Hydrogen and Fuel Cells in the Global Energy System. *Energy Environ. Sci.* **2019**, *12* (2), 463−491.

(2) Coduri, M.; Karlsson, M.; Malavasi, L. Structure-Property Correlation in Oxide-Ion and Proton Conductors for Clean Energy Applications: Recent Experimental and Computational Advancements. *J. Mater. Chem. A* **2022**, *10* (10), 5052−5110.

(3) Zhang, W.; Yashima, M. Recent Developments in Oxide Ion Conductors: Focusing on Dion-Jacobson Phases. *Chem. Commun.* **2022**, *59* (2), 134−152.

(4) Yaguchi, H.; Morikawa, D.; Saito, T.; Tsuda, K.; Yashima, M. High Oxide-Ion Conductivity through the Interstitial Oxygen Site in Sillén Oxychlorides. *Adv. Funct. Mater.* **2023**, *33* (27), No. 2214082, DOI: 10.1002/adfm.202214082.

(5) Morikawa, R.; Murakami, T.; Fujii, K.; Avdeev, M.; Ikeda, Y.; Nambu, Y.; Yashima, M. High Proton Conduction in $Ba_2LuAlO_5$ with Highly Oxygen-Deficient Layers. *Commun. Mater.* **2023**, *4* (1), No. 42.

(6) Shi, H.; Su, C.; Ran, R.; Cao, J.; Shao, Z. Electrolyte Materials for Intermediate-Temperature Solid Oxide Fuel Cells. *Prog. Nat. Sci. Mater. Int.* **2020**, *30* (6), 764−774.

(7) Rauf, S.; Zhu, B.; Yousaf Shah, M. A. K.; Tayyab, Z.; Attique, S.; Ali, N.; Mushtaq, N.; Wang, B.; Yang, C.; Asghar, M. I.; Lund, P. D. Application of a Triple-Conducting Heterostructure Electrolyte of $Ba_{0.5}Sr_{0.5}Co_{0.1}Fe_{0.7}Zr_{0.1}Y_{0.1}O_{3-\delta}$ and $Ca_{0.04}Ce_{0.80}Sm_{0.16}O_{2-\delta}$ in a High-Performance Low-Temperature Solid Oxide Fuel Cell. *ACS Appl. Mater. Interfaces* **2020**, *12* (31), 35071−35080.

(8) Fop, S.; Skakle, J. M. S.; McLaughlin, A. C.; Connor, P. A.; Irvine, J. T. S.; Smith, R. I.; Wildman, E. J. Oxide Ion Conductivity in the Hexagonal Perovskite Derivative $Ba_3MoNbO_{8.5}$. *J. Am. Chem. Soc.* **2016**, *138* (51), 16764−16769.

(9) Fop, S.; McCombie, K. S.; Wildman, E. J.; Skakle, J. M. S.; Irvine, J. T. S.; Connor, P. A.; Savaniu, C.; Ritter, C.; Mclaughlin, A. C. High Oxide Ion and Proton Conductivity in a Disordered Hexagonal Perovskite. *Nat. Mater.* **2020**, *19* (7), 752−757.

(10) Yashima, M.; Tsujiguchi, T.; Sakuda, Y.; Yasui, Y.; Zhou, Y.; Fujii, K.; Torii, S.; Kamiyama, T.; Skinner, S. J. High Oxide-Ion Conductivity through the Interstitial Oxygen Site in $Ba_7Nb_4MoO_{20}$-Based Hexagonal Perovskite Related Oxides. *Nat. Commun.* **2021**, *12* (1), No. 556.

(11) Suzuki, Y.; Murakami, T.; Fujii, K.; Hester, J. R.; Yasui, Y.; Yashima, M. Simultaneous Reduction of Proton Conductivity and Enhancement of Oxide-Ion Conductivity by Aliovalent Doping in $Ba_7Nb_4MoO_{20}$. *Inorg. Chem.* **2022**, *61* (19), 7537−7545.

(12) Murakami, T.; Shibata, T.; Yasui, Y.; Fujii, K.; Hester, J. R.; Yashima, M. High Oxide-Ion Conductivity in a Hexagonal Perovskite-Related Oxide $Ba_7Ta_{3.7}Mo_{1.3}O_{20.15}$ with Cation Site Preference and Interstitial Oxide Ions. *Small* **2022**, *18* (10), No. 2106785.

(13) Auckett, J. E.; Milton, K. L.; Evans, I. R. Cation Distributions and Anion Disorder in $Ba_3NbMO_{8.5}$ ($M$ = Mo, W) Materials: Implications for Oxide Ion Conductivity. *Chem. Mater.* **2019**, *31* (5), 1715−1719.

(14) García-González, E.; Parras, M.; González-Calbet, J. M. Crystal Structure of an Unusual Polytype: 7H-$Ba_7Nb_4MoO_{20}$. *Chem. Mater.* **1999**, *11* (2), 433−437.

(15) Fop, S.; Wildman, E. J.; Irvine, J. T. S.; Connor, P. A.; Skakle, J. M. S.; Ritter, C.; McLaughlin, A. C. Investigation of the Relationship

between the Structure and Conductivity of the Novel Oxide Ionic Conductor $Ba_3MoNbO_{8.5}$. *Chem. Mater.* **2017**, *29* (9), 4146−4152.
(16) Chambers, M. S.; Mccombie, K. S.; Auckett, J. E.; Mclaughlin, A. C.; Irvine, J. T. S.; Chater, P. A.; Evans, J. S. O.; Evans, I. R. Hexagonal Perovskite Related Oxide Ion Conductor $Ba_3NbMoO_{8.5}$: Phase Transition, Temperature Evolution of the Local Structure and Properties. *J. Mater. Chem. A* **2019**, *7* (44), 25503−25510.
(17) Yashima, M.; Tsujiguchi, T.; Fujii, K.; Niwa, E.; Nishioka, S.; Hester, J. R.; Maeda, K. Direct Evidence for Two-Dimensional Oxide-Ion Diffusion in the Hexagonal Perovskite-Related Oxide $Ba_3MoNbO_{8.5-\delta}$. *J. Mater. Chem. A* **2019**, *7* (23), 13910−13916.
(18) Fop, S.; Dawson, J. A.; Fortes, A. D.; Ritter, C.; McLaughlin, A. C. Hydration and Ionic Conduction Mechanisms of Hexagonal Perovskite Derivatives. *Chem. Mater.* **2021**, *33* (12), 4651−4660.
(19) Tansho, M.; Goto, A.; Ohki, S.; Mogami, Y.; Sakuda, Y.; Yasui, Y.; Murakami, T.; Fujii, K.; Iijima, T.; Yashima, M. Different Local Structures of Mo and Nb Polyhedra in the Oxide-Ion-Conducting Hexagonal Perovskite-Related Oxide $Ba_3MoNbO_{8.5}$ Revealed by $^{95}$Mo and $^{93}$Nb NMR Measurements. *J. Phys. Chem. C* **2022**, *126* (31), 13284−13290.
(20) Yasui, Y.; Tansho, M.; Fujii, K.; Sakuda, Y.; Goto, A.; Ohki, S.; Mogami, Y.; Iijima, T.; Kobayashi, S.; et al. Hidden Chemical Order in Disordered $Ba_7Nb_4MoO_{20}$ Revealed by Resonant X-Ray Diffraction and Solid-State NMR. *Nat. Commun.* **2023**, *14* (1), No. 2337.
(21) Sakuda, Y.; Murakami, T.; Avdeev, M.; Fujii, K.; Yasui, Y.; Hester, J. R.; Hagihala, M.; Ikeda, Y.; Nambu, Y.; Yashima, M. Dimer-Mediated Cooperative Mechanism of Ultrafast-Ion Conduction in Hexagonal Perovskite-Related Oxides. *Chem. Mater.* **2023**, *35* (22), 9774−9788.
(22) Yang, X.; Fernández-Carrión, A. J.; Wang, J.; Porcher, F.; Fayon, F.; Allix, M.; Kuang, X. Cooperative Mechanisms of Oxygen Vacancy Stabilization and Migration in the Isolated Tetrahedral Anion Scheelite Structure. *Nat. Commun.* **2018**, *9* (1), No. 4484.
(23) Karasulu, B.; Emge, S. P.; Groh, M. F.; Grey, C. P.; Morris, A. J. Al/Ga-Doped $Li_7La_3Zr_2O_{12}$ Garnets as Li-Ion Solid-State Battery Electrolytes: Atomistic Insights into Local Coordination Environments and Their Influence on $^{17}$O, $^{27}$Al, and $^{71}$Ga NMR Spectra. *J. Am. Chem. Soc.* **2020**, *142* (6), 3132−3148.
(24) Ma, S.; Ma, Y.; Zhang, B.; Tian, Y.; Jin, Z. Forecasting System of Computational Time of DFT/TDDFT Calculations under the Multiverse Ansatz via Machine Learning and Cheminformatics. *ACS Omega* **2021**, *6* (3), 2001−2024.
(25) Amoureux, J. P.; Fernandez, C. Triple, Quintuple and Higher Order Multiple Quantum MAS NMR of Quadrupolar Nuclei. *Solid State Nucl. Magn. Reson.* **1998**, *10* (4), 211−223.
(26) Amoureux, J. P.; Fernandez, C.; Steuernagel, S. Z Filtering in MQMAS NMR. *J. Magn. Reson., Ser. A* **1996**, *123* (1), 116−118.
(27) Amoureux, J. P.; Pruski, M. MQMAS NMR: Experimental Strategies and Applications. *Encycl. Magn. Reson.* **2007**, DOI: 10.1002/9780470034590.emrstm0319.pub2.
(28) Papulovskiy, E.; Shubin, A. A.; Terskikh, V. V.; Pickard, C. J.; Lapina, O. B. Theoretical and Experimental Insights into Applicability of Solid-State $^{93}$Nb NMR in Catalysis. *Phys. Chem. Chem. Phys.* **2013**, *15* (14), 5115−5131.
(29) Johnston, K. E.; Griffin, J. M.; Walton, R. I.; Dawson, D. M.; Lightfoot, P.; Ashbrook, S. E. $^{93}$Nb NMR and DFT Investigation of the Polymorphs of $NaNbO_3$. *Phys. Chem. Chem. Phys.* **2011**, *13* (16), 7565−7576.
(30) Kunwar, A. C.; Turner, G. L.; Oldfield, E. Solid-State Spin-Echo Fourier Transform NMR of $^{39}$K and $^{67}$Zn Salts at High Field. *J. Magn. Reson.* **1986**, *69* (1), 124−127.
(31) Engelhardt, G.; Kentgens, A. P. M.; Koller, H.; Samoson, A. Strategies for Extracting NMR Parameters from $^{23}$Na MAS, DOR and MQMAS Spectra. A Case Study for $Na_4P_2O_7$. *Solid State Nucl. Magn. Reson.* **1999**, *15* (3), 171−180.
(32) Iijima, T.; Kato, S.; Ikeda, R.; Ohki, S.; Kido, G.; Tansho, M.; Shimizu, T. Structure of Duplex Oxide Layer in Porous Alumina Studied by $^{27}$Al MAS and MQMAS NMR. *Chem. Lett.* **2005**, *34* (9), 1286−1287.
(33) Iijima, T.; Yamase, T.; Tansho, M.; Shimizu, T.; Nishimura, K. Electron Localization of Polyoxomolybdates with ε-Keggin Structure Studied by Solid-State $^{95}$Mo NMR and DFT Calculation. *J. Phys. Chem. A* **2014**, *118* (13), 2431−2441.
(34) Massiot, D.; Fayon, F.; Capron, M.; King, I.; Le Calvé, S.; Alonso, B.; Durand, J. O.; Bujoli, B.; Gan, Z.; Hoatson, G. Modelling One- and Two-Dimensional Solid-State NMR Spectra. *Magn. Reson. Chem.* **2002**, *40* (1), 70−76.
(35) Yasui, Y.; Tansho, M.; Fujii, K.; Sakuda, Y.; Goto, A.; Ohki, S.; Mogami, Y.; Iijima, T.; Kobayashi, S.; Kawaguchi, S.; Osaka, K.; Ikeda, K.; Otomo, T.; Yashima, M. Author Correction: Hidden Chemical Order in Disordered $Ba_7Nb_4MoO_{20}$ Revealed by Resonant X-Ray Diffraction and Solid-State NMR. *Nat. Commun.* **2023**, *14* (1), No. 4501.
(36) Kentgens, A. P. M.; Scholle, K. F. M. G. J.; Veeman, W. S. Effect of Hydration on the Local Symmetry around Aluminum in ZSM-5 Zeolites Studied by Aluminum-27 Nuclear Magnetic Resonance. *J. Phys. Chem. A* **1983**, *87* (22), 4357−4360.
(37) Hanna, J. V.; Pike, K. J.; Charpentier, T.; Kemp, T. F.; Smith, M. E.; Lucier, B. E. G.; Schurko, R. W.; Cahill, L. S. A $^{93}$Nb Solid-State NMR and Density Functional Theory Study of Four- and Six-Coordinate Niobate Systems. *Chem. - Eur. J.* **2010**, *16* (10), 3222−3239.


https://doi.org/10.1021/acs.jpcc.4c02645
J. Phys. Chem. C XXXX, XXX, XXX−XXX